Nanoscale Advances

PAPER

Check for updates

Sustainable carbon nanoarchitectonics: a biomass derived carbon nano-onion/magnetite composite as a reusable catalyst for solvent-free synthesis of benzoxazinones and benzthioxazinones

Gayathri Bindu Kurup, Prashanth Goud Banda, Emilin Francis and Raghasudha Mucherla *

In pursuit of greener and more sustainable chemical transformations, we report the synthesis of a biomass-derived carbon nano-onion/magnetite (CNO/Fe$_3$O$_4$) composite using flaxseed oil *via* a facile, eco-friendly wick pyrolysis method. The resulting nanocomposite exhibits excellent catalytic activity for the solvent-free synthesis of benzoxazinones and benzothioxazinones—pharmacologically relevant heterocycles—with yields of up to 95%. The unique layered architecture of CNOs combined with the magnetic functionality of Fe$_3$O$_4$ imparts high surface area, thermal stability, and magnetic recoverability, enabling easy separation and reuse over multiple cycles with minimal activity loss. Comprehensive characterization using FT-IR, XRD, BET, HR-TEM, FE-SEM, EDX, TGA, XPS, and VSM confirmed the structural integrity and composition of the hybrid catalyst. The methodology retains high efficiency at the gram scale, demonstrating its practical scalability. Overall, this study underscores the promise of biomass-derived nanocatalysts in advancing green chemistry through efficient, recyclable, and scalable catalytic systems for the synthesis of value-added compounds.

1 Introduction

Carbon nanoarchitectonics is an interdisciplinary field of materials science that is focused on the assembly and design of functional materials at the nanoscale using various carbon-based building blocks.[1,2] Drawing on insights from materials chemistry, this approach enables the development of materials with exceptional features including high specific surface area, tunable porosity, and excellent electrical conductivity.[3] Carbon allotropes can be tailored for innumerable uses such as energy storage, catalysis, and water purification, which emphasizes the importance of this approach in modern materials research.[4,5]

The field of carbon nanoarchitectonics comprises structures of varying dimensionality ranging from zero-dimensional to three-dimensional carbon nanostructures. These arrangements offer unique performance advantages depending on their morphology and targeted function.[6–9] A key advancement in this area is the development of hybrid and composite materials that integrate carbon nanomaterials with metals, polymers or ceramics, enabling synergistic enhancement of desired properties.[10–12] Such strategies are especially beneficial in

catalysis, where improved efficiency, stability and recyclability are essential. Additionally, the increasing focus on sustainability has propelled interest in biomass-derived carbon nano-architectures, which align with green chemistry principles.[5]

Among the diverse carbon nanostructures, Carbon Nano-Onions (CNOs) represent a particularly fascinating class.[13] These consist of concentric fullerene-like shells resembling onion layers and can be synthesized from sources such as graphite or carbon soot through methods like arc discharge, detonation and pyrolysis.[14,15] Among these, pyrolytic methods stand out for their simplicity, versatility, and high yield. Notably, the use of environmentally benign and renewable sources for CNO synthesis supports the dual goals of functional material production and ecological responsibility.[16]

Recent research has demonstrated significant progress in CNO synthesis from biomass sources. For instance, SungHoon Jung *et al.* (2020) utilized waste frying oil,[17] Suvam Nag Chowdhury *et al.* (2021) used diesel engine soot,[18] and Yunzi Xin *et al.* (2022) employed fish scales.[19] In 2023, Poonam Kumari extended this line of research using flaxseed oil,[20] followed by Jyothi Nallapureddy (2024) and Pooja Kadyan (2025), who used waste chicken fat[21] and flaxseed oil,[22] respectively. These efforts reflect the growing innovation in utilizing waste-derived precursors for nanomaterial synthesis.

Flaxseed oil (*Linum usitatissimum*) is a particularly promising precursor due to its rich content of oxygenated phenolic

Department of Chemistry, National Institute of Technology Warangal, Warangal-506 004, Telangana, India. E-mail: raghas13chem@nitw.ac.in; gb22cyr1r01@student.nitw.ac.in; prashanthb@student.nitw.ac.in; ef24cyr1r01@student.nitw.ac.in; Tel: +91 9550083100

compounds and fatty acids such as linoleic and oleic acid.[23,24] These constituents facilitate the formation of stable, high-surface-area CNOs with excellent dispersibility. The green synthesis of CNOs from flaxseed oil *via* wick pyrolysis serves as a compelling example of sustainable nanotechnology, offering both economic and environmental advantages.[25,26]

To enhance catalytic performance and ease of recovery, magnetically retrievable hybrid composites, such as CNO/Fe₃O₄, have garnered attention. Incorporating Fe₃O₄ nanoparticles imparts magnetic properties to the catalyst,[27–30] enabling facile separation from reaction mixtures *via* an external magnet.[31] This hybrid approach merges catalytic efficiency with operational convenience and contributes to cleaner reaction systems, consistent with green chemistry and sustainable practices.

In the realm of synthetic chemistry, one-pot multicomponent reactions (MCRs) have gained prominence for their atom economy, operational simplicity and ability to yield structurally diverse compounds. Among these, the synthesis of benzoxazinones and benzothioxazinones—heterocyclic frameworks with notable pharmaceutical relevance—is of particular interest. They possess multiple pharmacological activities, including the treatment of ulcers, high blood pressure, fungal infections, fever and inflammation.[32–34]

These compounds have traditionally been prepared using a one-pot strategy that combines three reactants *viz.*, 2-naphthol, an aldehyde, and urea or thiourea, catalyzed by a variety of agents. Reported catalysts include Lewis acids like FeCl₃·SiO₂,[35] Brønsted acids such as *p*-toluenesulfonic acid (PTSA)[36] and phosphomolybdic acid,[37] halogenated reagents like iodine and cyanuric chloride[38,39] and innovative systems such as thiamine hydrochloride,[40] pyridinium ionic liquids[41] and solid-supported catalysts like montmorillonite K10.[42] Although these methods are efficient, they often involve hazardous reagents, extended reaction durations, poor product yields and challenging catalyst recovery, thereby reducing their alignment with green chemistry principles.

To address these challenges, the present work reports a cost-effective, green methodology for synthesizing CNOs from flaxseed oil *via* wick pyrolysis, followed by *in situ* doping with Fe₃O₄. The resulting CNO/Fe₃O₄ composite functions as a heterogeneous catalyst for the synthesis of benzoxazinone and benzothioxazinone under solvent-free (neat) conditions, eliminating the need for hazardous solvents. This strategy enhances product yield and selectivity while simplifying catalyst recovery and minimizing environmental impact. Overall, it represents a significant step toward sustainable, scalable nanocatalysis using renewable resources for value-added chemical synthesis.

2 Experimental details

2.1 Material

Flaxseed oil (Indic Wisdom Wood Pressed), ferrous chloride (FeCl₂·4H₂O) (99%, Finar), ferric nitrate (Fe(NO₃)₃·9H₂O) (99%, Finar), ammonia solution (Sigma-Aldrich), ethanol (C₂H₅OH) (99%, Finar), *n*-hexane (98%, Finar), ethyl acetate (EtOAc) (99%, Finar), acetonitrile (99%, SDFCL), double distilled water, and cotton wick.

2.2 Preparation of CNOs

An economical and energy-efficient wick pyrolysis method was used to create CNOs.[17,25] A cotton wick was used to pyrolyze flaxseed oil in an oil lamp to synthesize CNOs, as schematically represented in Scheme 1. Carbon soot was collected by placing an inverted borosilicate glass beaker directly above the flame as shown in the scheme and also the images of the reaction setup are included in the SI (Fig. S24). To get rid of the unburnt aromatic residues and oil, the resulting soot was washed four to five times using hexane and acetonitrile.
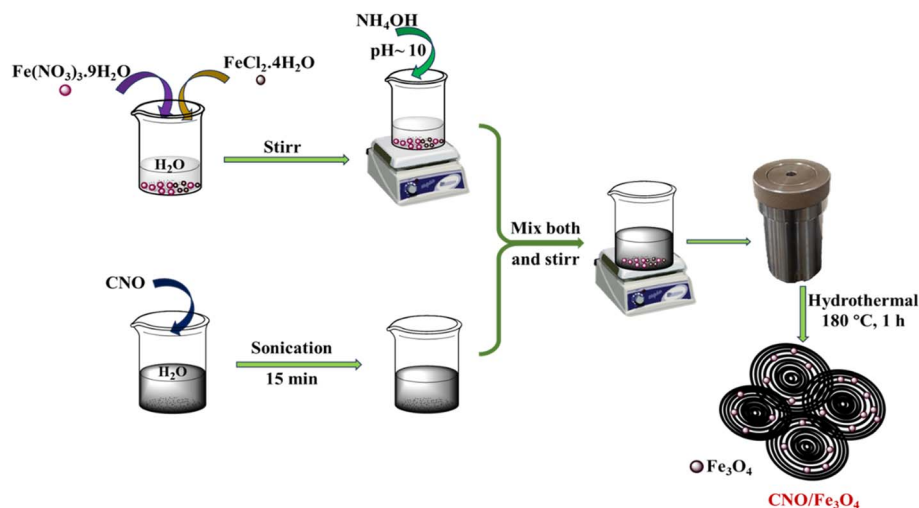
2.3 Preparation of CNO/Fe₃O₄ composite catalysts by the hydrothermal method

FeCl₂·4H₂O (1 mmol) and Fe(NO₃)₃·9H₂O (2 mmol), were taken into a beaker containing 50 mL of distilled water. The mixture
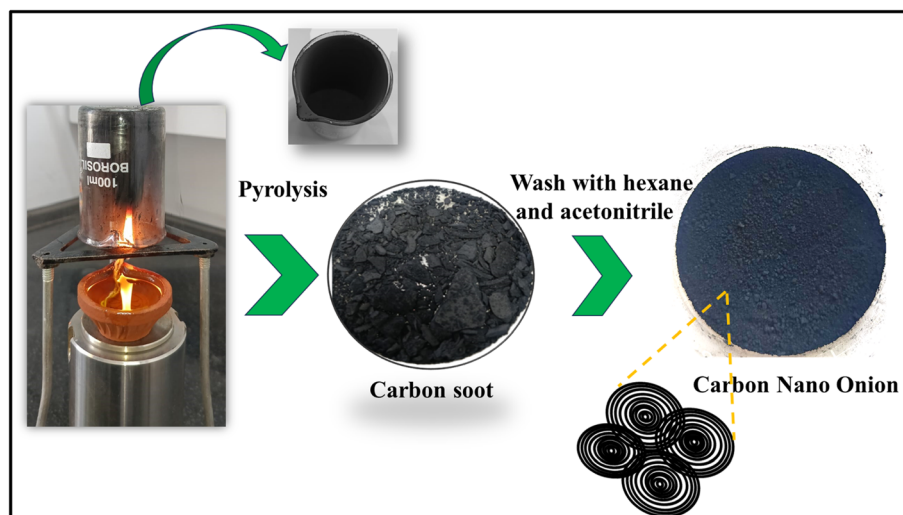
Scheme 1 Synthesis of CNOs by the wick pyrolysis method.

Scheme 2 Pictorial representation of the preparation of the CNO/Fe$_3$O$_4$ catalyst.

was stirred for 15 min and then NH$_4$OH was added to maintain the pH at ∼ 10.[43] Alongside in another beaker, 200 mg of CNOs was dispersed in 15 mL of distilled water and sonicated for 15 minutes. This dispersed CNO solution was poured into the beaker containing the precursors of Fe$_3$O$_4$ and stirred for 10 min for proper distribution of the components in the composite. This solution was poured into a Teflon-lined autoclave and kept inside a muffle furnace at 180 °C for 1 h. After cooling, the autoclave was taken out of the muffle furnace and separation of the black CNO/Fe$_3$O$_4$ product was achieved through magnetic extraction. Residual carbon was removed by sequential washing with distilled water and ethanol. The resulting material was dried in an oven, and then crushed with a spatula to obtain a fine powder, which was reported as the CNO/Fe$_3$O$_4$ composite catalyst. The pictorial representation of the catalyst preparation is shown in Scheme 2.

2.4 General synthetic method for benzoxazinones and benzothioxazinones

The CNO/Fe$_3$O$_4$ catalyzed synthesis of benzoxazinones and benzothioxazinones was achieved through a one-pot condensation of 2-naphthol, aldehyde (1 : 1 molar ratio), and urea/thiourea (1.2 eq.) at 120 °C under neat conditions. Post-reaction, EtOAc and water were used to carry out the workup of the mixture. The EtOAc portion was passed over Na$_2$SO$_4$ and then evaporated to produce a crude product. Silica gel column chromatography was then used to purify the product, which was analysed by ^{1}H and ^{13}C NMR spectral analyses, as shown in the SI (Fig. S4–S23).

2.5 Characterization of the catalyst

The structural properties of the synthesized materials were analyzed using several characterization techniques. Powder X-ray diffraction (PXRD) studies were carried out using Ni-filtered Cu K radiation (λ = 1.5406 Å) in a 2θ scan range of 5°–100° using a PAN Analytical Advance X-ray diffractometer to

confirm the phase conformation of the catalyst. FTIR spectra of the synthesized catalyst were recorded using a PerkinElmer spectrometer within the range of 4000 to 400 cm^{-1}, employing the KBr pellet technique to investigate its molecular structure and composition. Raman spectra of the catalyst were recorded using a Wasatch Photonics Raman 785 ER compact spectrometer to identify molecular vibrations and confirm catalyst composition through characteristic spectral peaks. The surface morphology, grain size, particle size distribution, and crystallinity of the CNO/Fe$_3$O$_4$ catalyst were examined using field emission scanning electron microscopy (FE-SEM, JEOL/JSM-IT800), transmission electron microscopy (TEM) and selected area electron diffraction (SAED) with a JEOL/JEM-2100 TEM instrument. X-ray photoelectron spectroscopy (Physical Electronics, PHI 5000 Versa Probe III) was used to measure the binding energies of the components in the CNO/Fe$_3$O$_4$ catalyst. To gain a deeper insight into the catalyst's magnetic behaviour, hysteresis loops (M–H curves) were obtained using a vibrating sample magnetometer (VSM, Lake Shore, 8600 Series). Thermogravimetric analysis (TGA) was performed with a TA Instruments SDT Q600 thermal analyzer, ranging from 30–800 °C at a heating rate of 10 °C per minute, to assess the stability of the catalyst. The catalyst's pore volume and surface area were analyzed using Brunauer–Emmett–Teller (BET, Quantachrome Instruments). ^{1}H and ^{13}C NMR spectra of the synthesized organic compounds were obtained on a Bruker Avance III 400 MHz NMR spectrometer, using DMSO-d$_6$ as the solvent and tetramethylsilane (TMS) as the internal reference. High-resolution mass spectrometry (HRMS) was conducted with an Agilent Q-TOF 6230 to confirm the mass of the selected target product.

3 Results and discussion

3.1 Preparation of the CNO/Fe$_3$O$_4$ catalyst

CNO was prepared by the wick pyrolysis method from flaxseed oil (Scheme 1) and mixed with the precursor solution of Fe$_3$O$_4$.

The resulting mixture was subjected to hydrothermal reaction at 180 °C for 1 h to get the catalyst. The step-by-step catalyst preparation is depicted in Scheme 2.

3.2 Characterization of the CNO/Fe₃O₄ catalyst

The PXRD patterns reveal two characteristic peaks for CNOs as evident from Fig. 1a(i). The peak at $2\theta = 25.06°$ represents hexagonal graphitic carbons, and the peak at $2\theta = 44.66°$ indicates sp^3-bonded carbon.

In Fig. 1a(ii), the CNO/Fe₃O₄ composite displays distinct peaks at $2\theta = 30.4°, 35.6°, 43.2°, 53.8°, 57.2°$, and $63.1°$, which correspond to the Fe₃O₄ reflection planes (220), (311), (400), (422), (511), and (440), respectively along with the presence of peaks of CNO. The observed diffraction peaks closely match that of pure Fe₃O₄ in Fig. 1a (JCPDS card no. 75-0033) conforming its phase purity.[43] The presence of characteristic CNO peaks suggests successful grafting within the composite. The average crystallite sizes were calculated using the Scherrer equation as 0.55 nm for the CNOs and 3.67 nm for the CNO/Fe₃O₄ composite.

The FTIR spectrum of CNO, illustrated in Fig. 1b(i), displays several peaks corresponding to different bond vibrations.
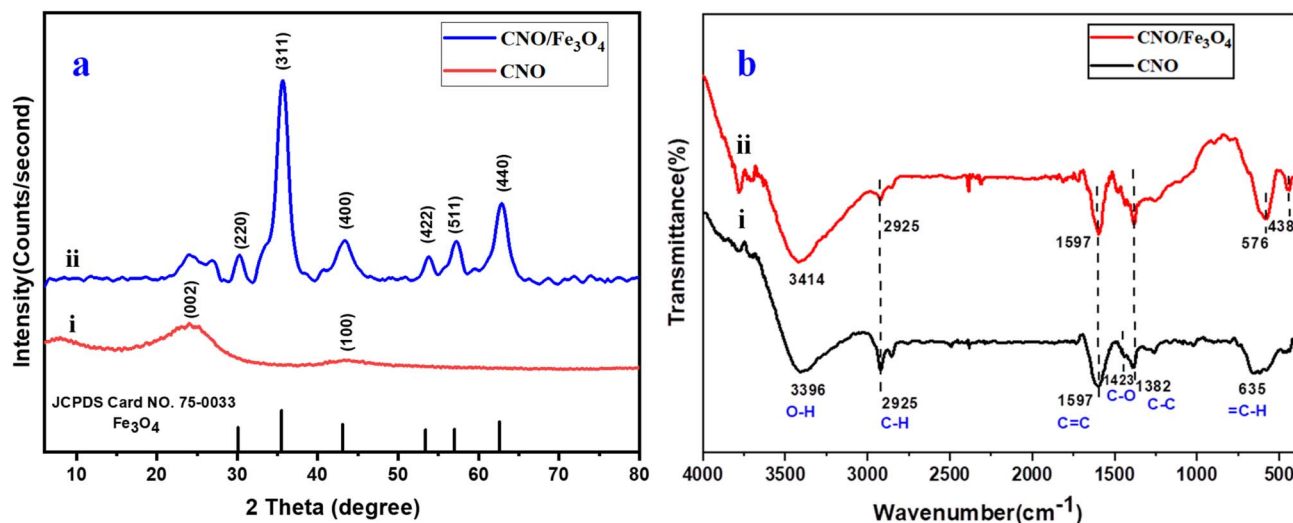
Fig. 1 (a) PXRD patterns of (i) CNO and (ii) CNO/Fe₃O₄. (b) FTIR spectra of (i) CNO and (ii) CNO/Fe₃O₄.
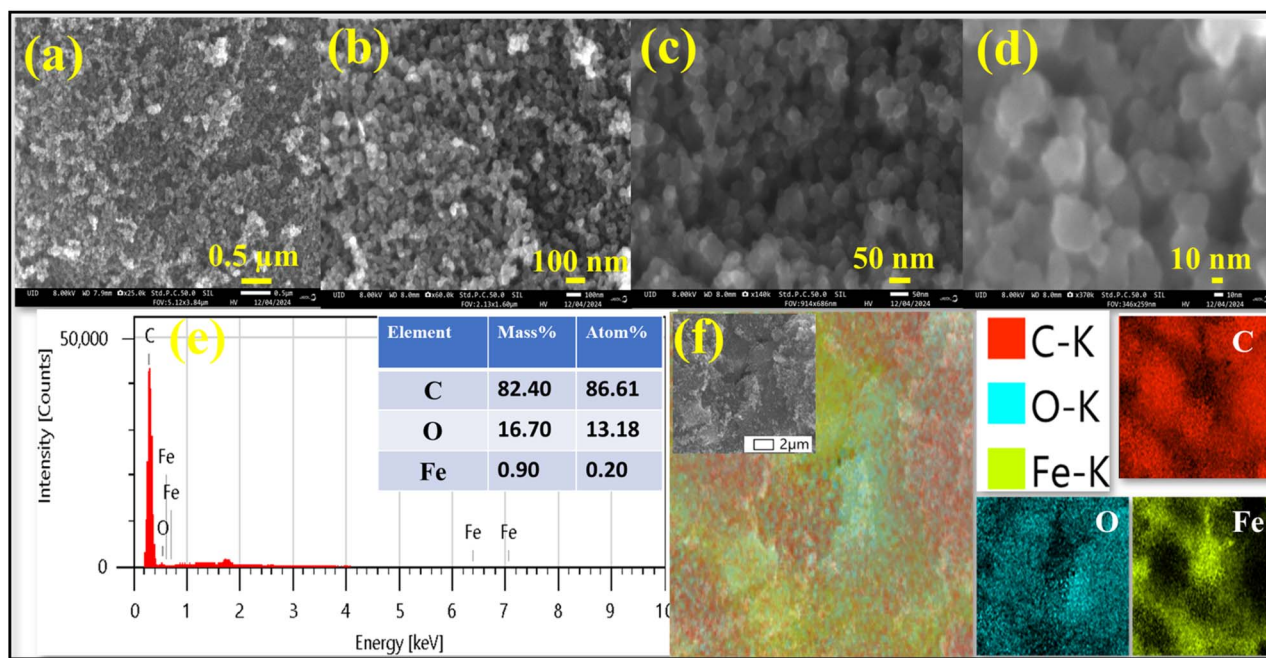

Fig. 2 FESEM images at different magnification: (a) 500 nm, (b) 100 nm, (c) 50 nm and (d) 10 nm, (e) EDX data and (f) elemental mapping of CNO/Fe₃O₄.

Specifically, the peak at 635 cm^{-1} represents =CH bending vibrations, while the peaks at 1382 cm^{-1} and 1423 cm^{-1} are attributed to C–C and C–O stretching vibrations, respectively. The peak at 1597 cm^{-1} is related to C=C stretching, and the peak at 2925 cm^{-1} reflects C–H stretching vibrations.

Additionally, the peak at 3396 cm^{-1} is ascribed to O–H stretching vibrations, confirming the existence of hydroxyl groups. For the CNO/Fe$_3$O$_4$ composite, shown in Fig. 1b(ii), all the characteristic peaks of CNO are retained, with additional peaks at 438 cm^{-1} and 576 cm^{-1} corresponding to Fe–O
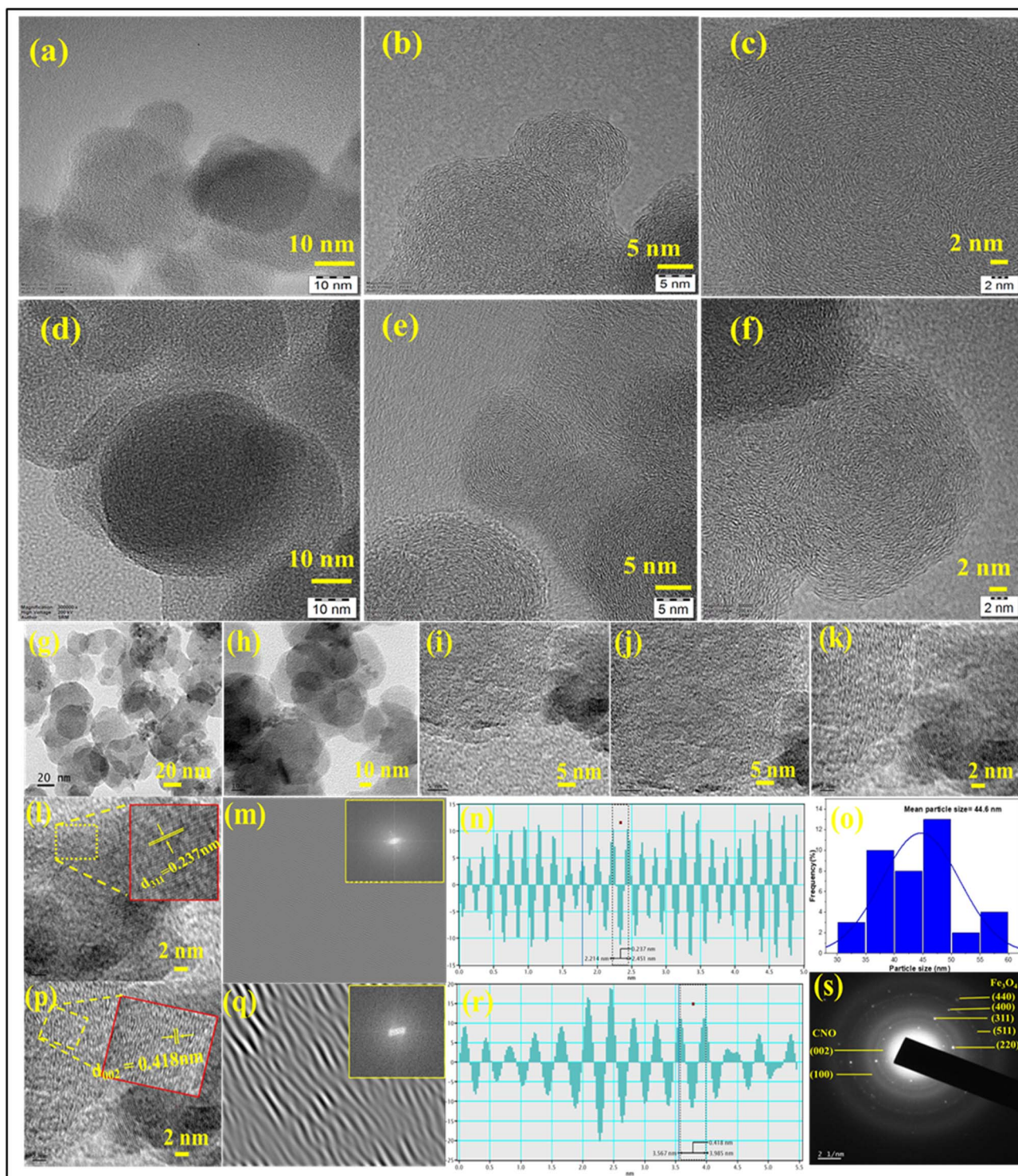
Fig. 3 HR-TEM images at different magnifications: (a–c) CNO and (d–k) CNO/Fe$_3$O$_4$, (l) HR-TEM image at 2 nm with the Fe$_3$O$_4$ plane, (m) IFFT image & inset FFT of image (l), (n) line profile of image (l), (o) size distributions of CNO/Fe$_3$O$_4$, (p) HR-TEM images at 2 nm resolution with the CNO plane, (q) IFFT image & inset FFT of image (p), (r) line profile of image (p), and (s) SAED pattern of CNO/Fe$_3$O$_4$.

stretching vibrations at tetrahedral and octahedral sites, characteristic of the magnetite structure.[44,45] Together, the FTIR and PXRD analyses provide an integrated understanding of the chemical structure and composition of both CNO and CNO/Fe_3O_4.

The Raman spectra of CNO and CNO/Fe_3O_4 reveal distinct spectral differences, as shown in SI Fig. S1. The Raman peaks at 1233 cm^{-1} and 1575 cm^{-1} in CNO correspond to the disorder band (D-band) and the graphitic band (G-band), respectively. The D-band originates from defects or structural disorder in the carbon framework, whereas the G-band corresponds to the in-plane vibrations of sp^2-hybridized carbon atoms. In the case of CNO/Fe_3O_4, the peaks shift to 1309 cm^{-1} (D-band) and 1516 cm^{-1} (G-band), which likely indicates an interaction between CNO and Fe_3O_4, altering the vibrational modes of the carbon atoms. These shifts suggest changes in the structural and electronic environment due to the incorporation of Fe_3O_4. The intensity ratio (I_D/I_G) was 0.86 for CNO and increased to 0.94 for CNO/Fe_3O_4, implying that the addition of Fe_3O_4 enhances the disorder or defect density within the carbon structure. This change highlights the impact of Fe_3O_4

incorporation on the material's intrinsic properties and structural organization.

Topography of synthesised CNO/Fe_3O_4 was studied using FESEM. Fig. 2a, b, c and d depicts FESEM images at different magnifications of 500 nm, 100 nm, 50 nm and 10 nm respectively, showing an agglomerated structure due to the magnetic attraction of Fe_3O_4 in the composite. The EDX (Fig. 2e) data and elemental mapping (Fig. 2f) prove the existence of elements C, O and Fe within the material and show the elemental distribution of different elements within the sample across an area of 2 μm. The weight percentages of C, O and Fe are 82.40%, 16.70% and 0.90% respectively as presented in the inset table of Fig. 2e.

High-Resolution Transmission Electron Microscopy (HR-TEM) serves as an exceptional method for investigating the atomic-scale resolution, internal structure, particle size, and crystallinity of catalysts. Fig. 3a, b and c presents HR-TEM images of the synthesized CNO at magnifications of 10 nm, 5 nm and 2 nm, respectively. Fig. 3d–f shows HR-TEM images of the CNO/Fe_3O_4 catalyst at the same magnifications. Additionally, Fig. 3g–k displays HR-TEM images of the CNO/Fe_3O_4
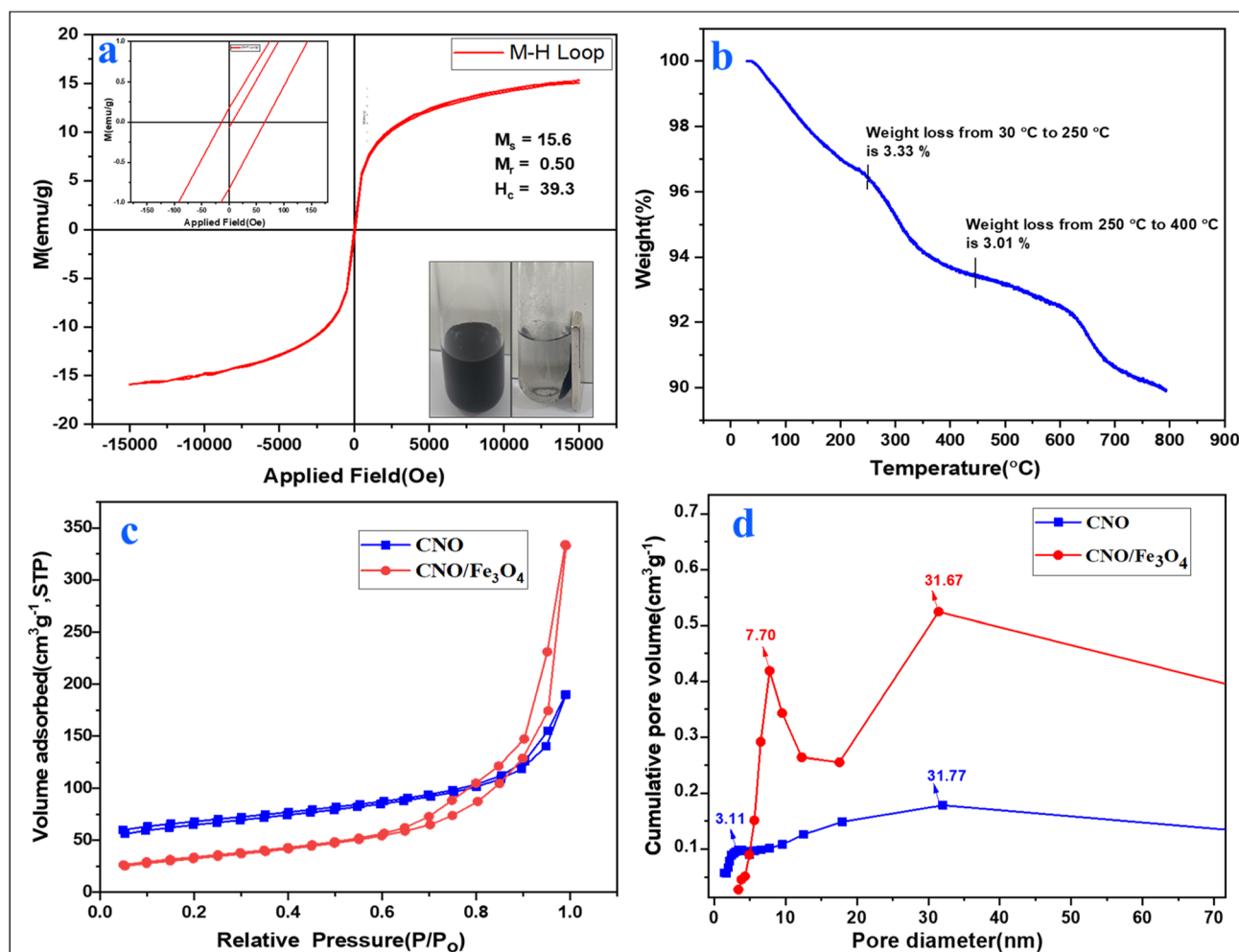

Fig. 4   (a) Hysteresis curve, (b) TGA curve for CNO/Fe_3O_4, (c) N_2 adsorption/desorption isotherm and (d) pore size distribution curve of CNO and CNO/Fe_3O_4.

catalyst captured from different areas at magnifications 20 nm, 10 nm, 5 nm and 2 nm.

The observed particle agglomeration is likely due to the magnetic interactions between nanoparticles caused by the Fe_3O_4 in the catalyst. Lattice fringe measurements, as depicted in Fig. 3l, show a d-spacing of 0.237 nm, pertaining to the (311) lattice plane and aligning with PXRD data. Statistical image analysis, illustrated in Fig. 3o, indicates a mean particle size of 44.6 nm confirming the nano nature of the catalyst. Additionally, the selected area electron diffraction (SAED) ring pattern shown in Fig. 3s highlights the polycrystalline nature of the catalyst.

Fig. 3m and n further includes inverse fast Fourier transform (IFFT) and line profile images respectively, which confirm the lattice fringes of Fe_3O_4 on the catalyst surface, with a d-spacing of 0.237 nm. Similarly, Fig. 3q and r feature the IFFT and line profile images of CNO on the catalyst surface, revealing a d-spacing of 0.418 nm corresponding to the lattice plane (002). These outcomes provide detailed insights into the structural characteristics of the CNO/Fe_3O_4 catalyst.

The hysteresis curves of the synthesized CNO/Fe_3O_4 catalyst were recorded at room temperature under a 15 000 Oe magnetic field using a VSM, as shown in Fig. 4a. The curve indicates significant magnetic properties of the catalyst, with a remanence (M_r) of 0.50 emu g^{-1}, coercivity (H_c) of 39.3 Oe, and saturation magnetization (M_s) of 15.6 emu g^{-1}. The narrow hysteresis loop, as seen in Fig. 4a, confirms the catalyst's soft magnetic nature.

To assess the thermal stability of the CNO/Fe_3O_4 catalyst under reaction conditions, TGA was conducted in a nitrogen atmosphere. As shown in Fig. 4b, a two-stage decomposition pattern emerged with increasing temperature. The first weight loss of 3.33% in the 30–250 °C range is likely due to the evaporation of physisorbed moisture and solvents from the catalyst's
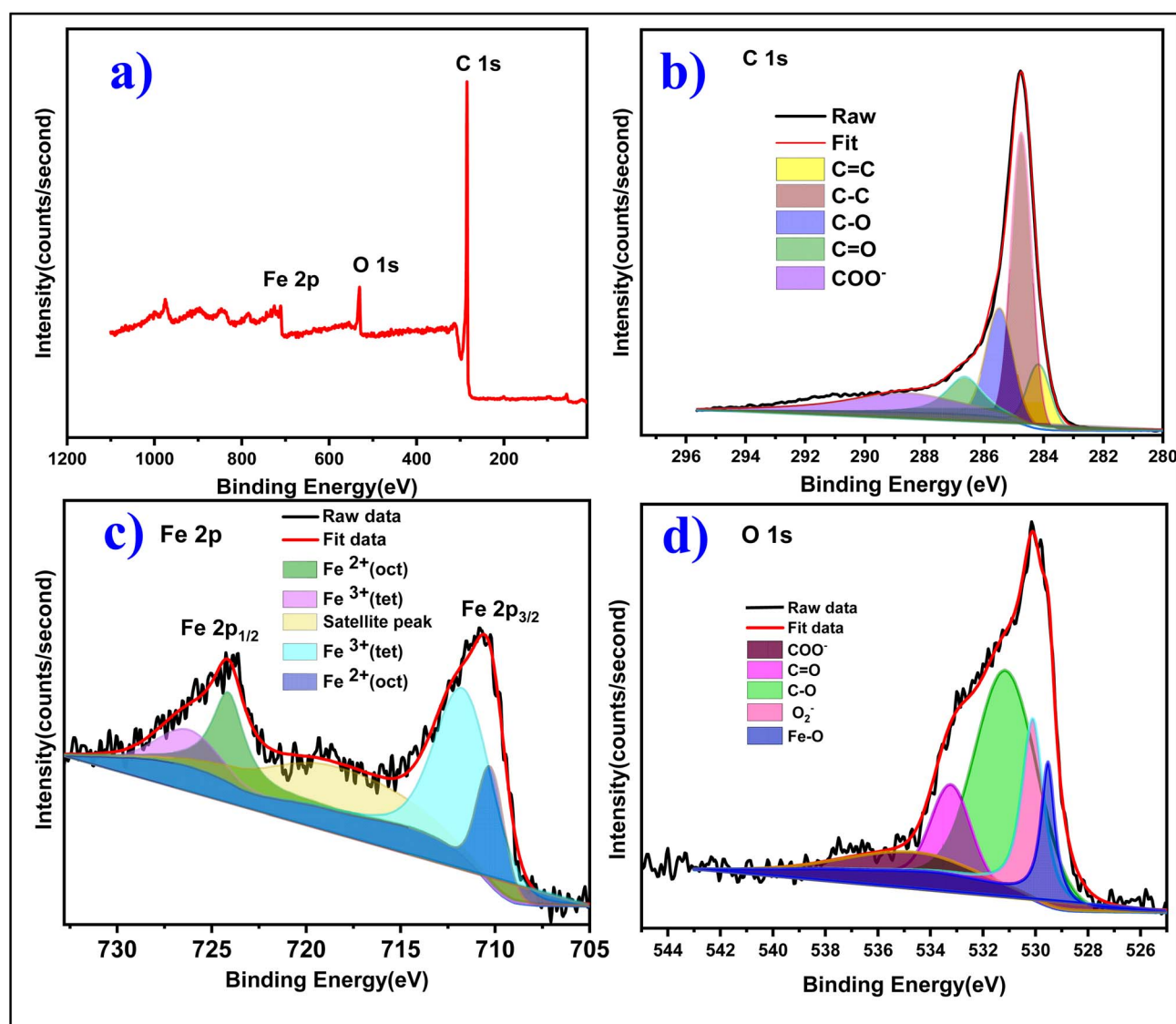

Fig. 5 XPS spectra of CNO/Fe_3O_4 (a), XPS full spectrum of the CNO/Fe_3O_4 catalyst (b), C 1s HR-XPS profile (c), Fe 2p HR-XPS profile and (d) O 1s HR-XPS profile.

surface. The second weight loss of 3.01% in the 250–400 °C range may result from the breakdown of the catalyst's functional organic moieties. The residual weight of 89.92% for the CNO/Fe_3O_4 nanocatalyst indicates its superior thermal stability, particularly at the reaction temperature, confirming the catalyst's stability.

The Brunauer–Emmett–Teller (BET) method is commonly utilized in gas adsorption–desorption analysis which plays a crucial role in assessing the porosity and specific surface area of catalysts that are important for several applications. From the N_2 adsorption–desorption isotherms illustrated in Fig. 4c, it is evident that CNO and the CNO/Fe_3O_4 composite exhibit type-IV isotherms. The BET surface area of pristine CNO was found to be 204.6 m^2 g^{-1}, while the CNO/Fe_3O_4 composite showed a reduced surface area of 113.84 m^2 g^{-1} confirming successful composite formation. The observed reduction in surface area for the composite can be attributed to the aggregation of Fe_3O_4 nanoparticles and partial pore blocking within the CNO matrix. Additionally, surface coverage and structural densification during synthesis likely contribute to the diminished BET surface area. Nevertheless, the composite still offers enhanced catalytic performance due to synergistic interactions between the carbon-based matrix and the metal oxide component.

The Barrett–Joyner–Halenda (BJH) analysis reveals average pore diameters of 5.15 nm and 18.09 nm for CNO and CNO/Fe_3O_4 respectively, within a pore diameter range of 2.5–35 nm as evident from Fig. 4d confirming their mesoporous nature. From the BJH data, the total pore volume of 0.261 cm^3 g^{-1} for CNO and 0.515 cm^3 g^{-1} for the CNO/Fe_3O_4 composite suggests that the composite, despite its lower surface area compared to pristine CNO possesses enhanced pore accessibility for potential catalytic applications (the results are summarized in Table S3).

The XPS analysis assesses the electronic states and surface composition of the CNO/Fe_3O_4 catalyst. As shown in Fig. 5a, the XPS full survey scan for the CNO/Fe_3O_4 catalyst is presented. The HR-XPS profile of C 1s in Fig. 5b reveals five deconvoluted peaks at approximately 284.1 eV, 284.7 eV, 285.5 eV, 286.6 eV and 288.8 eV, attributed to C=C, C–C, C–O, C=O and COO^- binding energies, respectively. The HR-XPS profile of Fe 2p within the Fe_3O_4 matrix, displayed in Fig. 5c, shows two peaks representing Fe $2p_{1/2}$ and Fe $2p_{3/2}$. Upon deconvolution of each Fe 2p peak, two spectral bands at binding energies of 726.4 eV and 711.5 eV were seen that are ascribed to the $2p_{1/2}$ and $2p_{3/2}$ of Fe^{3+} species in tetrahedral sites, respectively. Additionally, Fe^{2+}

species in octahedral sites may account for the binding energies of the other two peaks at 723.9 eV and 710.2 eV. The O 1s spectral band, depicted in Fig. 5d, displays binding energies of 529.4 eV, 530 eV, 531.1 eV, 533.23 eV and 535.9 eV, representing Fe–O, O_2^-, C–O, C=O and COO^-, respectively.

3.3 Application of CNO/Fe_3O_4 in the synthesis of benzoxazinones and benzothioxazinones

This study highlights the application of magnetically separable CNO/Fe_3O_4 nanoparticles as a heterogeneous catalyst for the multicomponent synthesis of benzoxazinones and benzothioxazinones under neat conditions. The reaction involves 2-naphthol, aldehydes, and urea/thiourea, showcasing the versatility and potential efficiency of this catalyst in advancing green chemistry methodologies. For the model reaction depicted in Fig. 6, 2-naphthol (1 mmol), anisaldehyde (1 mmol), urea (1.2 mmol) and 25 mg of catalyst were used under the specified conditions to produce benzoxazinone. Motivated by the encouraging preliminary outcomes and comprehensive catalyst characterization, further investigations were carried to evaluate the influence of critical reaction parameters such as solvent choice, temperature variations and catalyst loading. The objective was to optimize the reaction conditions and establish an efficient protocol for synthesizing benzoxazinones and benzothioxazinones.

The initial experiments were focused on examining the impact of various solvents on the reaction. The model reaction was first conducted in toluene with a 1 : 1 : 1.2 molar ratio of 2-naphthol, aryl aldehyde and urea/thiourea, in the absence of the catalyst at 120 °C. However, the reaction exhibited minimal progress even after a prolonged duration of 24 hours. In subsequent trials, the addition of small amounts of CNO/Fe_3O_4 nanocatalyst moderately improved the reaction rate, highlighting its critical role in synthesizing benzoxazinones and benzothioxazinones. During optimization, the reaction was performed with different solvents and also under neat conditions for a duration of 2 h and the yield of the purified isolated product is depicted in Table 1. In nonpolar aprotic solvents such as toluene (Entry 1), a yield of 88% was achieved. Polar protic solvents like water, methanol and ethanol afforded yields of 69%, 65% and 68%, respectively (Entries 2–4). Polar aprotic solvents, including DCM, THF, acetonitrile, acetone, DMF and DMSO, yielded products at 85%, 82%, 80%, 52%, 33% and 44% (Entries 5–8), respectively. However, the best results were obtained under neat conditions, confirming its effectiveness for
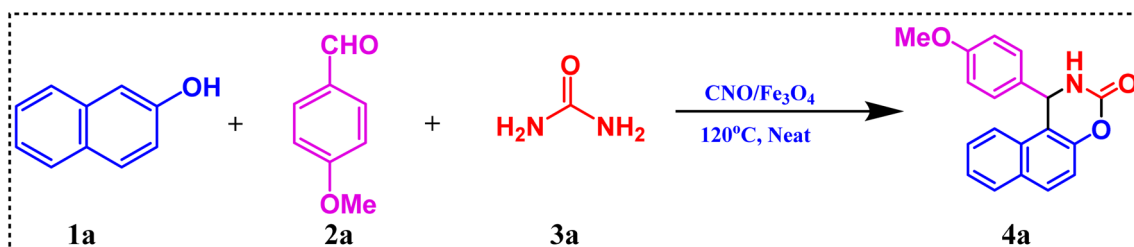

Fig. 6 Model reaction for the synthesis of benzoxazinones.

Table 1 Optimization of solvent[a]

Entry	Solvent	Yield%
1	Toluene	88
2	Water	69
3	Methanol	65
4	Ethanol	68
5	DCM	85
6	THF	82
7	Acetonitrile	80
8	Acetone	52
9	DMF	30
10	DMSO	44
11	**Neat**	**95**

[a] Reaction conditions: 2-naphthol (1 mmol), anisaldehyde (1 mmol) and urea (1.2 mmol), 25 mg of catalyst, 120 °C.

the reaction. After establishing the neat conditions, the reaction time was optimized by monitoring the disappearance of the aldehyde spot and appearance of the product spot on TLC. It was established that the model reaction completed efficiently within 45 minutes.

To enhance the reaction rate, the influence of temperature was thoroughly examined. Based on the data shown in Fig. 7a, increasing the temperature significantly improved the reaction rate with the best product yield achieved at 120 °C, within 45 minutes under neat conditions. For temperature optimization, the reaction was performed at 80 °C, 100 °C, 120 °C and 140 °C, resulting in product yields of 55%, 89%, 95% and 95%, respectively as shown in Fig. 7a. From these results, it can be concluded that 120 °C is the most appropriate temperature for the reaction.

Given the critical role of the catalyst in the synthesis of benzoxazinones and benzothioxazinones, the effect of varying catalyst amounts in the model reaction was carefully evaluated, as shown in Fig. 7b. The results indicate that 25 mg (6.7 wt%) of catalyst, under 1 mmol reactant conditions with a molar ratio of **1a : 2a : 3a** = 1 : 1 : 1.2, achieves the best yield of benzoxazinones (calculation of product yield for the model reaction is shown in SI Table S1). Catalyst optimization, as shown in the figure,

demonstrates that using 15 mg (4.1 wt%), 20 mg (5.4 wt%), 25 mg (6.7 wt%), 30 mg (7.9 wt%), and 35 mg (9.1 wt%) leads to product yields of 85%, 90%, 95%, 95%, and 93%, respectively. From this analysis, it can be concluded that 25 mg (6.7 wt%) is the optimal catalyst amount.

The catalytic performance of pristine CNO, CNO/Fe$_3$O$_4$, and bare Fe$_3$O$_4$ (prepared *via* the co-precipitation method) was evaluated for this model reaction as part of a control experiment under the optimized reaction conditions for 1 h, yielding the products at 44%, 95%, and 29% respectively. These results demonstrate that CNO/Fe$_3$O$_4$ exhibits the highest catalytic activity compared to the individual components as catalysts (Table S2). This superior activity is attributed to the synergistic effect of CNO and Fe$_3$O$_4$, enhancing the catalyst's efficiency. Remarkably, this integration not only reduced the reaction time to 45 minutes but also improved the yield to 95%, highlighting CNO/Fe$_3$O$_4$ as an optimal nanocatalyst for this synthesis.

Satisfied with the initial results under the optimized reaction parameters, the scope of this methodology was broadened by employing various substituted aromatic and heteroaromatic aldehydes as substrates for the synthesis of benzoxazinones and benzothioxazinones (**4a–4q**) as shown in Table 2. From the table it is evident that aryl aldehydes bearing electron-donating groups (EDGs) furnished the corresponding products in good to excellent yields with an accelerated reaction rate compared to unsubstituted benzaldehyde. In contrast, substrates with electron-withdrawing groups (EWGs) also gave good yields but required longer reaction times. It may be because, presence of an EDG enhances the reactivity and yield, while an EWG reduces it due to electronic and steric effects. In the reaction, the increased electron density stabilizes the intermediate formed during the condensation and cyclization steps, leading to a more efficient reaction pathway and higher yield. Additionally, the position of the substituent can influence steric hindrance and electronic effects, further affecting the reaction efficiency and yield. For heteroaromatic aldehydes like furfural, prolonged reaction times were necessary to obtain satisfactory yields of the corresponding benzoxazinones. Benzoxazinones gave better yields than benzothioxazinones which may be due to
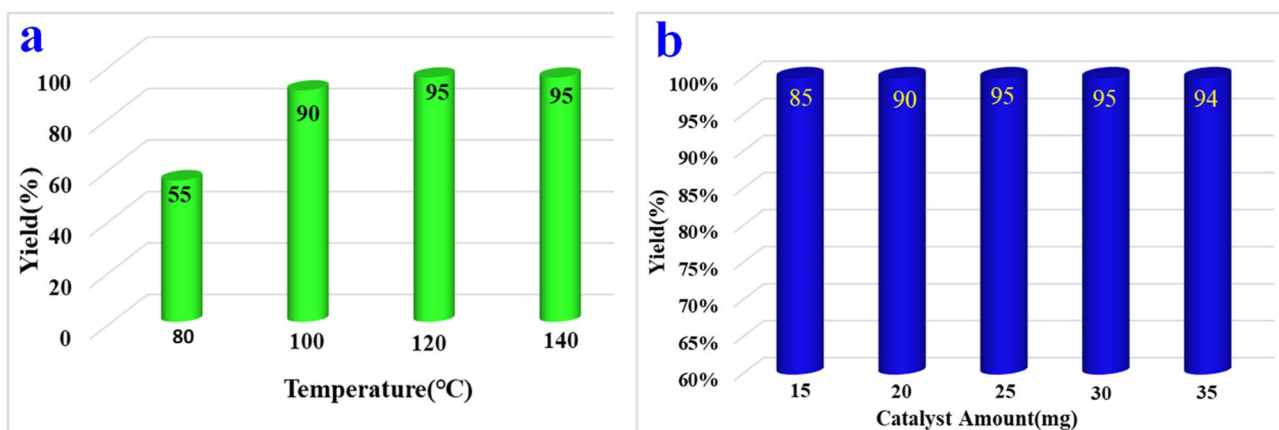

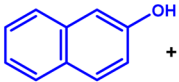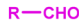**Fig. 7** (a) Optimization of temperature and (b) optimization of catalyst amount.
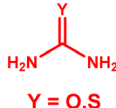
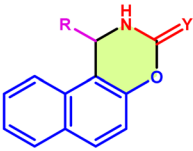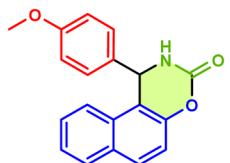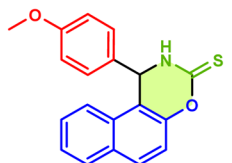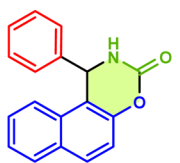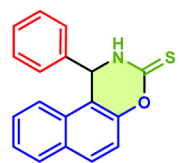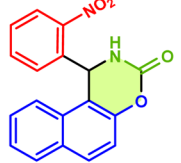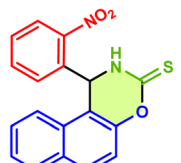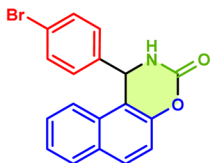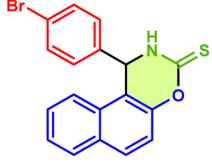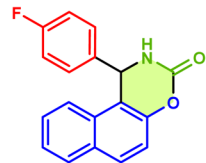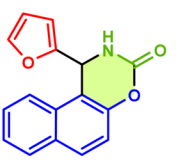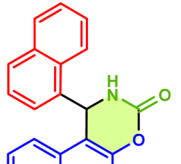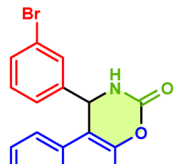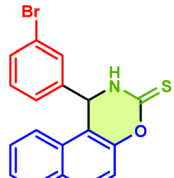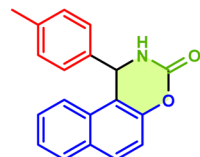the larger size and less electronegative nature of sulfur compared to oxygen. The larger atomic size of sulfur introduce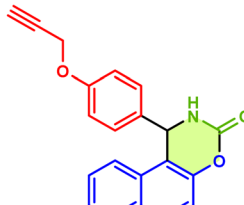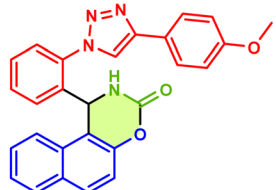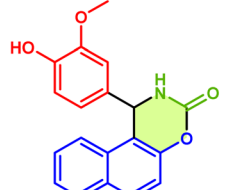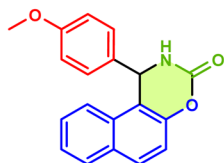s steric hindrance, which could impact cyclization efficiency during the reaction. This might result in slightly lower yields for the benzothioxazinone. To the best of our knowledge, the compound **4p** from the benzoxazinone derivative series in Table 2 is a novel one.

The gram scale reaction was performed using 1 g of 2-naphthol, anisaldehyde (0.84 mL), urea (0.5 g) and 150 mg

catalyst at 120 °C under neat conditions, achieving a commendable yield of 75% within 45 minutes. Although this yield is slightly lower than the 95% yield obtained in the smaller-scale experiments, it remains impressive for a larger-scale process, highlighting the efficiency of this method. This reduction in yield is common during scale-up and could be attributed to factors such as heat distribution or mixing efficiency.

Table 2 Substrate scope of benzoxazinone and benzthioxazinone catalysed by CNO/Fe$_3$O$_4$[a]

4a, 95% — 45 min

4b, 88% — 45 min

4c, 91% — 55 min

4d, 87% — 75 min

4e, 85% — 50 min

4f, 80% — 60 min

4g, 92% — 50 min

4h, 85% — 70 min

4i, 90% — 60 min

4j, 84% — 75 min

4k, 90% — 60 min

4l, 89% — 50 min

4m, 80% — 75 min

4n, 94% — 45 min

4o, 88% — 80 min

4p, 82% — 120 min

4q, 70% — 120 min

Gram scale synthesis of product 4a : 75%

[a] Reaction conditions: 2-naphthol (1 mmol), anisaldehyde (1 mmol) and urea (1.2 mmol), 25 mg of catalyst, 120 °C.

The reaction progress was tracked by thin-layer chromatography (TLC), monitoring the disappearance of the aldehyde spot and the formation of the product. All known products were successfully isolated and purified. Additionally, the identity of the products was established through ^{1}H NMR and ^{13}C NMR analyses for all compounds, while the HRMS spectral data was used for selected compounds (as provided in the SI).

3.3.1 Recyclability of the catalyst. The recyclability of the biomass-derived CNO/Fe$_3$O$_4$ composite catalyst was evaluated through multiple catalytic cycles to establish its durability and efficiency, as shown in Fig. 8. After each reaction, the composite catalyst was effortlessly recovered using an external magnet, owing to its considerable magnetic properties. It was subsequently washed, dried and reused. The catalytic performance remained almost consistent over at least five consecutive cycles (drop in product yield from 95% to 85%), demonstrating the material's robust stability and reusability. This excellent recyclability emphasises the practicality and environmental sustainability of the CNO/Fe$_3$O$_4$ composite, making it a promising candidate for green and scalable synthetic applications. The results further emphasize the potential of such novel nanomaterials to minimize waste and reduce operational costs in industrial processes.
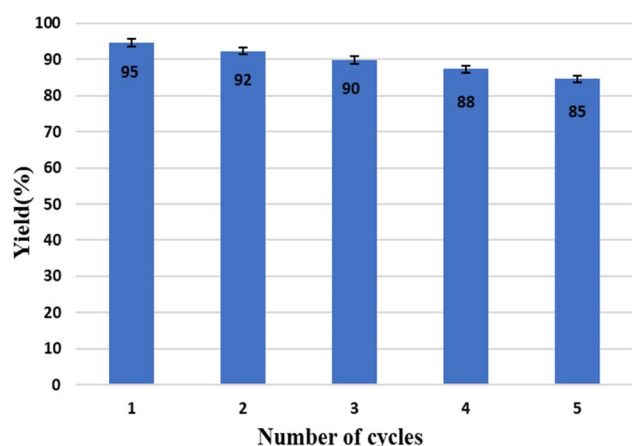

Fig. 8 Recyclability test of the catalyst CNO/Fe$_3$O$_4$.

PXRD and FTIR analyses were carried out to examine the structural stability of the recycled CNO/Fe$_3$O$_4$ catalyst and the results are shown in the SI. Similar diffraction peaks were observed in PXRD and FTIR patterns of fresh (Fig. 1a and b) and recovered catalysts (Fig. S2 and S3), suggesting that the structure of CNO/Fe$_3$O$_4$ does not change even after five reaction cycles.

The catalytic efficiency of the synthesized CNO/Fe$_3$O$_4$ composite was evaluated against previously reported catalysts for the synthesis of benzoxazinone and benzthioxazinone, as summarized in Table 3. The catalyst, montmorillonite K10 (Entry 1) achieves a good product yield of 89% at 160 °C under neat conditions in 30 minutes, combining decent yield with moderate reaction time. Moving on, zinc triflate (Entry 2) operates under reflux conditions in CH$_3$CN for 300 minutes, producing a moderate product yield of 82%, with the long reaction time and toxic solvent reducing its practicality. Similarly, zinc oxide (Entry 3) provides a product yield of 85% at 150 °C under neat conditions in 90 minutes, thus limiting its efficiency owing to its longer reaction time. TMSCl/NaI (Entry 4) achieves a lower product yield of 78% at 140 °C in a solvent mixture of DMF and CH$_3$CN for 120 minutes, highlighting its limitations in both yield and reaction conditions. H$_{14}$[NaP$_5$W$_{30}$O$_{110}$]/SiO$_2$ (Entry 5) gives a high product yield of 91%, requiring 60 minutes under reflux in ethanol but its separability and reusability are limited due to its complex nature. The catalyst RuCl$_2$(PPh$_3$)$_3$ (Entry 6) demonstrates a better product yield of 93%, requiring 900 minutes under reflux in toluene, making it less practical due to long reaction time and lack of reusability. Guanidine hydrochloride (Entry 7) achieves a yield of 88% at 140 °C under neat conditions in 70 minutes, showing moderate efficiency. Cellulose sulfuric acid (Entry 8) provides a similar high yield of 92% at a lower temperature of 80 °C in water with SDS, but the reaction stretches over a prolonged 180 minutes. Fe$_3$O$_4$ (Entry 9) achieves a product yield of 90% under reflux in toluene for 12 hours, showcasing good performance but with extended reaction time and harsh conditions. MgFe$_2$O$_4$@SiO$_2$–HSO$_3$ (Entry 10) is a magnetically reusable catalyst that achieves a 97% product yield in just 4 minutes at 120 °C under microwave irradiation. However, the reliance on microwave heating presents

Table 3 Comparison of the catalytic activity of CNO/Fe$_3$O$_4$ with some literature reports on the synthesis of benzoxazinone and benzthioxazinone

| Entry	Catalyst	Reaction condition	Time (min)	Yield%	References
1	Montmorillonite K10	160 °C/solvent free	30	89	42
2	Zinc triflate	Reflux/CH$_3$CN	300	82	46
3	Zinc oxide	150 °C/solvent free	90	85	47
4	TMSCl/NaI	140 °C/DMF + CH$_3$CN	120	78	48
5	H$_{14}$[NaP$_5$W$_{30}$O$_{110}$]/SiO$_2$	Reflux/EtOH	60	91	49
6	RuCl$_2$(PPh$_3$)$_3$	Reflux/toluene	900	93	50
7	Guanidine hydrochloride	140 °C/solvent free	70	88	51
8	Cellulose sulfuric acid	80 °C/water + SDS	180	92	52
9	Fe$_3$O$_4$	Reflux/toluene	12 h	90	53
10	MgFe$_2$O$_4$@SiO$_2$–HSO$_3$	Microwave (120 °C)/solvent free	4 min	97	54
11	**CNO/Fe$_3$O$_4$**	**120°C/solvent free**	**45**	**95**	**This work**
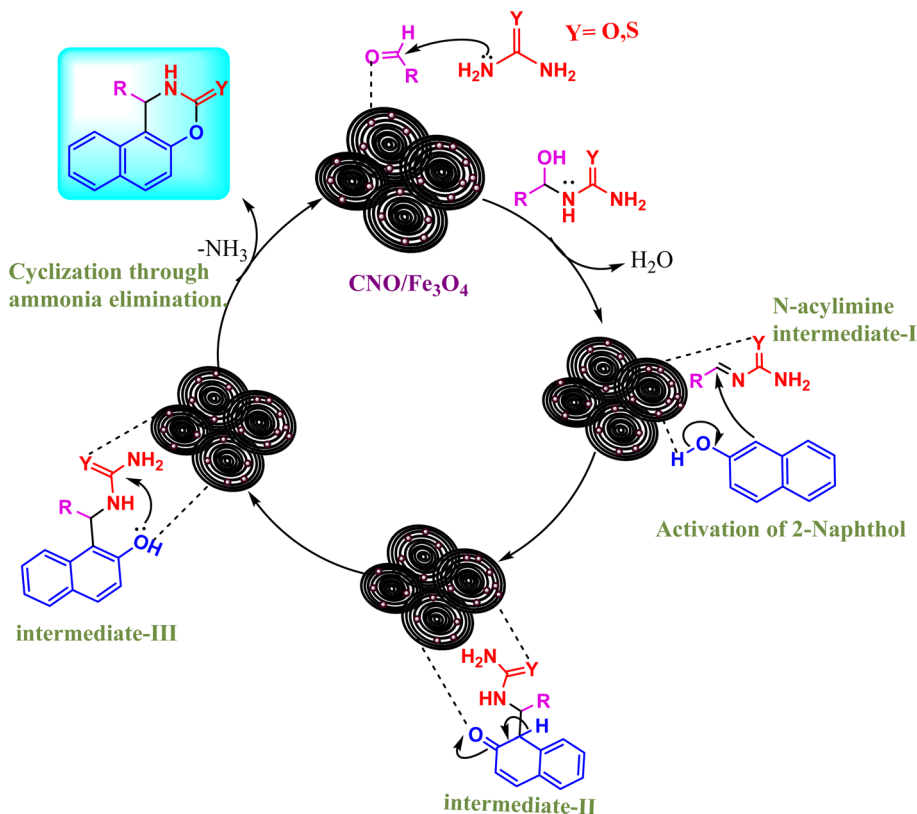
Fig. 9 Plausible mechanism of CNO/Fe$_3$O$_4$ in the synthesis of benzoxazinones and benzthioxazinones.

challenges for industrial scale-up due to equipment limitations. Additionally, the catalyst synthesis involves hazardous sulfonation steps, which do not align with green chemistry principles. Among the catalysts evaluated, CNO/Fe$_3$O$_4$ (Entry 11) exhibited the highest efficiency, affording a 95% yield at 120 °C under neat conditions within 45 minutes using conventional heating. Notably, the catalyst is derived from flaxseed oil, a renewable biomass source, aligning well with the principles of green chemistry. Thus, the catalyst comparison highlights the superior performance of CNO/Fe$_3$O$_4$, which delivers high yields in a shorter reaction time under mild, eco-friendly conditions, demonstrating significant advantages over other catalysts.

3.3.2 Plausible mechanism of CNO/Fe$_3$O$_4$ in the synthesis of benzoxazinones and benzthioxazinones. Based on previous literature reports,[54–56] Fig. 9 illustrates the plausible mechanism of CNO/Fe$_3$O$_4$ in facilitating the synthesis of benzoxazinone and benzthioxazinone through catalytic interactions. The reaction begins with the condensation of an aldehyde with urea/thiourea in the presence of catalyst. This step proceeds through the nucleophilic attack of the amine group on the aldehyde carbonyl, leading to the *in situ* formation of *N*-acylimine intermediate-I. For experimental validation of the pathway, the crude reaction mixture was collected after 15 minutes of the model reaction and analysed by FTIR and NMR spectroscopy. The spectral data included in Fig. S26 strongly suggest the successful formation of *N*-acylimine (intermediate-I) during the progress of the reaction. This intermediate plays a pivotal role

in the subsequent reaction sequence. Under the optimized reaction conditions, the catalyst activates 2-naphthol by deprotonating its hydroxyl group, enhancing its nucleophilicity. This activation facilitates the reaction with the *N*-acylimine intermediate-I. The activated naphthol undergoes a nucleophilic attack on the electrophilic carbon of the *N*-acylimine intermediate-I. This step forms intermediate-II, incorporating both the naphthol and the aldehyde-derived moieties. Aromatization of the intermediate occurs through the migration of an α-proton which stabilizes the structure by forming an aromatic ring resulting in intermediate-III. Cyclization *via* the elimination of ammonia (NH$_3$) in intermediate-III facilitates the formation of the final heterocyclic compound and the catalyst is recovered with the aid of an external magnet. NH$_3$ formation in the last step was validated through multiple qualitative tests and supporting images are provided in the SI (Fig. S25).

4 Conclusion

This work demonstrates the green synthesis of a carbon nano-onion/magnetite (CNO/Fe$_3$O$_4$) hybrid nanocatalyst using flaxseed oil *via* wick pyrolysis. The composite exhibited high catalytic efficiency in the one-pot, solvent-free synthesis of benzoxazinone and benzothioxazinone derivatives—important heterocycles with pharmaceutical relevance. The concentric-layered structure of CNOs, combined with the magnetic functionality of Fe$_3$O$_4$, contributes to high surface area, thermal

robustness, and excellent magnetic recoverability. The catalyst retained activity over at least five reaction cycles with negligible loss in performance, highlighting its reusability. A gram-scale reaction (1 g of 2-naphthol) at 120 °C produced a 75% yield in 45 minutes, confirming its potential for scale-up. Although marginally lower than the 95% yield achieved on a smaller scale, this performance reinforces the catalytic system's efficiency and adaptability for practical, larger-scale applications. Overall, this study offers an economical and sustainable platform for the synthesis of value-added heterocycles, promoting the broader use of biomass-derived nanomaterials in green chemistry and catalysis.

Conflicts of interest

There are no declared conflicts.

Data availability

The data supporting this article have been included as part of the supplementary information (SI). Supplementary information: Raman spectra of catalyst; PXRD, FTIR spectra of recycled catalyst; NMR spectra and data of synthesized compounds. See DOI: https://doi.org/10.1039/d5na00674k.

Acknowledgements

References

1 K. Ariga, Q. Ji, W. Nakanishi, J. P. Hill and M. Aono, *Mater. Horiz.*, 2015, **2**, 406–413.

2 K. Ariga, Y. Yamauchi, G. Rydzek, Q. Ji, Y. Yonamine, K. C. W. Wu and J. P. Hill, *Chem. Lett.*, 2014, **43**, 36–68.

3 X. Chen, C. Li, M. Grätzel, R. Kostecki and S. S. Mao, *Chem. Soc. Rev.*, 2012, **41**, 7909–7937.

4 X. Qu, P. J. J. Alvarez and Q. Li, *Water Res.*, 2013, **47**, 3931–3946.

5 R. Li, Y. Zhou, W. Li, J. Zhu and W. Huang, *Research*, 2020, **2020**, 1–27.

6 S. K. Mandal, S. Mandal and D. Jana, *Graphene and its Derivatives (Volume 2) Water/Wastewater Treatment and Other Environmental Applications*, Springer, 2023, pp. 151–172.

7 C. Zhu and S. Dong, *Functional Graphene-Based Nanomaterials: Rational Synthesis*, ed. X. Zhang, Springer, 2019, pp. 451–496.

8 X. Huang, X. Qi, F. Boey and H. Zhang, *Chem. Soc. Rev.*, 2012, **41**, 666–686.

9 S. Iijima, *Nature*, 1991, **354**, 56–58.

10 M. F. El-Kady, V. Strong, S. Dubin and R. B. Kaner, *Science*, 2012, **335**, 1326–1330.

11 S. Hyun, A. Sivanantham and S. Shanmugam, *Nanocarbons Energy Convers. Supramol. Approaches*, 2019, pp. 455–496.

12 D. Chen, H. Feng and J. Li, *Chem. Rev.*, 2012, **112**, 6027–6053.

13 D. Ugarte, *Nature*, 1992, **359**, 707–709.

14 X. Li, H. Wang, H. Chen, Q. Zheng, Q. Zhang, H. Mao, Y. Liu, S. Cai, B. Sun and C. Dun, *Chem*, 2020, **6**, 933–944.

15 A. Guo, K. Bao, S. Sang, X. Zhang, B. Shao, C. Zhang, Y. Wang, F. Cui and X. Yang, *RSC Adv.*, 2021, **11**, 6850–6858.

16 N. S. Alsaiari, F. M. Alzahrani, A. Amari, H. Osman, H. N. Harharah, N. Elboughdiri and M. A. Tahoon, *Molecules*, 2023, **28**, 463.

17 S. Jung, Y. Myung, G. S. Das, A. Bhatnagar, J.-W. Park, K. M. Tripathi and T. Kim, *New J. Chem.*, 2020, **44**, 7369–7375.

18 S. N. Chowdhury, T. T. Tung, Q. T. H. Ta, M. Castro, J. F. Feller, S. K. Sonkar and K. M. Tripathi, *New J. Chem.*, 2021, **45**, 3675–3682.

19 Y. Xin, K. Odachi and T. Shirai, *Green Chem.*, 2022, **24**, 3969–3976.

20 P. Kumari, K. M. Tripathi, K. Awasthi and R. Gupta, *Environ. Sci. Pollut. Res.*, 2023, **30**, 71048–71062.

21 J. Nallapureddy, T. V. M. Sreekanth, M. R. Pallavolu, P. S. Srinivasa Babu, R. R. Nallapureddy, J. H. Jung and S. W. Joo, *ACS Appl. Mater. Interfaces*, 2024, **16**, 23334–23343.

22 P. Kadyan, S. Sharma, K. Sharma, R. K. Sharma, V. Singh and S. Grover, *J. Mater. Sci.: Mater. Electron.*, 2025, **36**, 1–21.

23 A. Goyal, V. Sharma, N. Upadhyay, S. Gill and M. Sihag, *J. Food Sci. Technol.*, 2014, **51**, 1633–1653.

24 M. Z. Koçak, *Processes*, 2024, **12**, 689.

25 D. Mohapatra, S. Badrayyana and S. Parida, *Mater. Chem. Phys.*, 2016, **174**, 112–119.

26 K. M. Tripathi, T. S. Tran, Y. J. Kim and T. Kim, *ACS Sustain. Chem. Eng.*, 2017, **5**, 3982–3992.

27 G. B. Kurup, P. G. Banda, S. Gubbala, E. S. Bindiya, S. G. Bhat and R. Mucherla, *J. Inorg. Organomet. Polym. Mater.*, 2025, **35**, 1730–1742.

28 G. Aravind, M. Raghasudha, D. Ravinder, A. Gaffoor and V. Nathanial, *J. Nanostruct. Chem.*, 2015, **5**, 77–83.

29 M. Raghasudha, D. Ravinder and P. Veerasomaiah, *J. Magn. Magn. Mater.*, 2016, **420**, 45–50.

30 P. G. Banda, G. B. Kurup and R. Mucherla, *J. Phys. Chem. Solids*, 2023, **181**, 111556.

31 P. G. Banda and R. Mucherla, *ACS Omega*, 2022, 7, 36233–36244.

32 M. Bahmanziyari and H. Naeimi, *New J. Chem.*, 2025, **49**, 865–876.

33 S. Huang, Y. Pan, Y. Zhu and A. Wu, *Org. Lett.*, 2005, 7, 3797–3799.

34 M. Yadav, M. Dutta, P. Tanwar, R. Jain, A. Srivastava, R. K. Sharma and C. Microw, *Chem*, 2021, **8**, 96–116.

35 M. A. Ghasemzadeh and J. Safaei-Ghomi, *Iran. J. Catal.*, 2024, **6**, 3.

36 M. Dabiri, A. S. Delbari and A. Bazgir, *Heterocycles*, 2007, **71**, 543–548.

37 A. Chaskar, V. Vyavhare, V. Padalkar, K. Phatangare and H. Deokar, *J. Serb. Chem. Soc.*, 2011, **76**, 21–26.

38 M. Sharma, S. Manohar and D. S. Rawat, *J. Heterocycl. Chem.*, 2012, **49**, 589–595.

39 F. Nemati and A. Beyzai, *J. Chem.*, 2013, **2013**, 365281.

40 M. Lei, L. Ma and L. Hu, *Synth. Commun.*, 2011, **41**, 3424–3432.

41 F. Dong, Y. Li-fang and Y. Jin-ming, *Res. Chem. Intermed.*, 2013, **39**, 2505–2512.

42 M. Kumar, S. Sharma, K. Thakur, O. S. Nayal, V. Bhatt, M. S. Thakur, N. Kumar, B. Singh and U. Sharma, *Asian J. Org. Chem.*, 2017, **6**, 342–346.

43 M. M. Ba-Abbad, A. Benamour, D. Ewis, A. W. Mohammad and E. Mahmoudi, *JOM*, 2022, **74**, 3531–3539.

44 L. Nalbandian, E. Patrikiadou, V. Zaspalis, A. Patrikidou, E. Hatzidaki and C. N. Papandreou, *Curr. Nanosci.*, 2016, **12**, 455–468.

45 S. D. Lawaniya, S. Kumar, Y. Yu and K. Awasthi, *Sci. Rep.*, 2024, **14**, 7904.

46 A. Hajra, D. Kundu and A. Majee, *J. Heterocycl. Chem.*, 2009, **46**, 1019–1022.

47 G. B. D. Rao, M. P. Kaushik and A. K. Halve, *Tetrahedron Lett.*, 2012, **53**, 2741–2744.

48 G. Sabitha, K. Arundhathi, K. Sudhakar, B. S. Sastry and J. S. Yadav, *J. Heterocycl. Chem.*, 2010, **47**, 272–275.

49 A. Gharib, B. R. H. Khorasani, M. Jahangir and M. Roshani, *Bulg. Chem. Commun.*, 2013, **45**, 59–63.

50 X. Zhu and Y. R. Lee, *Bull. Korean Chem. Soc.*, 2012, **33**, 3831–3834.

51 A. Olyaei, M. Sadeghpour and M. Zarnegar, *Chem. Heterocycl. Compd.*, 2013, **49**, 1374–1377.

52 A. Kumar, M. K. Gupta and M. Kumar, *RSC Adv.*, 2012, **2**, 7371–7376.

53 N. Basavegowda, K. B. S. Magar, K. Mishra and Y. R. Lee, *New J. Chem.*, 2014, **38**, 5415–5420.

54 N. G. Salunkhe, C. A. Ladole, N. V. Thakare and A. S. Aswar, *Res. Chem. Intermed.*, 2018, **44**, 355–372.

55 S. Khabnadideh, A. solhjoo, R. Heidari, L. Amiri Zirtol, A. Sakhteman, Z. Rezaei, E. Babaei, S. Rahimi and L. Emami, *BMC Chem.*, 2022, **16**, 1–18.

56 P. Rahmani and F. K. Behbahani, *Inorg. Nano-Met. Chem.*, 2017, **47**, 713–716.